Hybrid Carrier-Based Virtual-Space-Vector Coordinate-Driven PWM Strategy of Three-Level T-type NPC Converters for Electric Aircraft Propulsion Applications

Feng Guo, *Member*, *IEEE*, Zhuxuan Ma, *Student Member*, *IEEE*, Fei Diao, *Student Member*, *IEEE*, Yue Zhao, *Senior Member, IEEE,* and Patrick Wheeler, *Fellow, IEEE*

***Abstract*—Green airborne transportation driven by the state-of-the-art turboelectric propulsion technology has received considerable attention from the aviation industry. To generate electrified thrust, three-level neutral-point-clamped (3L-NPC) converter-fed motor drives are the most promising candidate for the powertrain of future aircraft. However, the neutral-point (NP) potential fluctuation and deviation lead to harmonics and imperil the lifespan of semiconductors and capacitors. Besides, excessive power losses on the converter limiting propulsive power shorten the flight distance. To solve these issues, a new hybrid modulation strategy is proposed in this paper. With respect to the takeoff and climbing featuring NP voltage drift-prone regions, carrier-based (CB) coordinate-driven modulation waves enabling virtual-space-vector (VSV) are exploited. As for those operating points with high power factor at the cruise, by reconstructing modulation waves, not only can the NP voltage balance be realized, but also the switching loss is reduced by active discontinuous pulse trains. The less computational burden is attributed to implementations in the sextant-coordinate system. The effectiveness of the proposed algorithm is verified by simulation results from a Simulink/PLECS model and experimental results obtained from a 200 kVA silicon-carbide (SiC) based T-type 3L-NPC prototype with a variable output fundamental frequency.**

***Index Terms*—Capacitor voltage balance, electric aircraft propulsion, hybrid coordinate modulation, three-level.**

I. Introduction

With the mega development of next-generation airborne transportation, electric aircraft propulsion technologies are solutions to realizing significantly reduced carbon footprint and nitrogen oxide emissions, better flight experience, and lower maintenance costs [1]-[3]. Aggressive targets have been set over the past decade to improve aviation's impact on the environment. For example, the EU's Flightpath 2050 program dedicates to lowering the CO_2 and NO_x per passenger kilometer by 75% and 90%, respectively and reduce noise emissions by 65%, compared with those capabilities in the year 2000 [4]. Also, many research projects have been carried out globally, for example, NASA's N3-X [5], Airbus E-Fan X [6], and another NASA's new aircraft design, named STARC-ABL [7].

Power electronics converters have become a key enabler for aircraft powertrain electrification. Following the study on the electric starter/generator (ESG) demonstrator [8], an advanced aircraft turboelectric distributed propulsion (TeDP) architecture is presented in this paper, aiming at higher penetration of the electrical system to drive the main engine turbine blades in the startup instead of using the auxiliary power unit (APU). As shown in Fig.1, two integrated ESG systems incorporating a permanent magnet synchronous machine (PMSM) and a bi-directional converter take power from the main engine via high

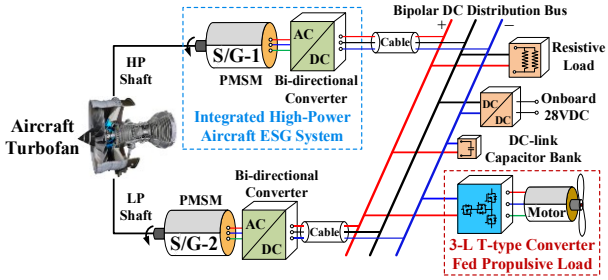

Fig. 1. Schematic overview of the advanced aircraft TeDP system.

pressure (HP) shaft and low pressure (LP) shaft. The onboard loads are interfaced with high-power ESGs via an electric power system (EPS). Though ± 270 V is the highest voltage standard for current aircraft, the use of medium-voltage dc distribution (MVDC), such as ± 1.5 kV for E-Fan X and ± 2 kV for N3-X, is a future trend due to the more lightweight power cable. For the designed TeDP system, a bipolar dc-bus structure of ± 540 V is chosen as a candidate so that the requirement of propulsive and non-propulsive loads can be fulfilled at the same time. Considering the reduced *dv/dt* and lower voltage stress [9], the three-level (3-L) converter rather than the two-level (2-L) counterpart is selected to drive the MW-class motor. In addition, its increased equivalent switching frequency is helpful for output power quality in high-speed drives with up to kilohertz fundamental frequency. In this work, the silicon-carbide (SiC) based 3-L T-type converter (3-L T^2C) shown in Fig.2 is selected as the high-power propulsion drive, which has a lower number of semiconductor devices compared with the 3-L active-neutral-point-clamped converter [10].

As the 3-L T^2C serves as the interface between the EPS and the propulsion motor, its performance has a significant impact on the efficiency and reliability of the propulsion drives. An inherent issue of the 3-L topology, however, is the neutral-point (NP) voltage imbalance rendered by the split dc-link, which can overstress the capacitors, and switching devices and lead to excessive harmonics. While the drift can be restored by itself, the performance highly depends on system parameters and harmonic orders [11]. To correct the shifted potential in the NP, the pulse-wide-modulation (PWM) method emerges as a simple but powerful alternative, without compromising on stringent requirements of volume and size in aerospace applications.

In the existing literature, numerous advanced PWM schemes have been studied for the 3L-NPC topology on the premise of capacitor voltage balance. In general, these strategies can be classified as space-vector modulation (SVM) and carrier-based PWM (CBPWM) by the principle of pulse train generation. Quite a few SVM variants evolve from the concept of the nearest-three-vector (NTV) and the nearest-three-virtual-vector (NTV^2). The NTV features the center-aligned seven-segment

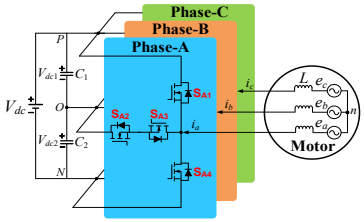

Fig. 2. Schematic of 3LT^{2}C-fed electric propulsion motor.

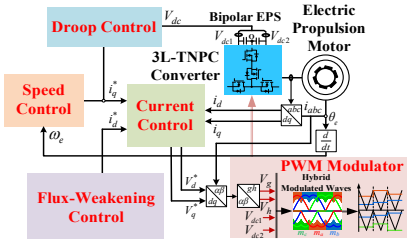

Fig. 3. Control blocks of the developed TeDP system.

switching pattern. However, the adoption of medium vectors results in undesirable low-frequency NP voltage fluctuation, particularly for high modulation index (MI) and low load power factor (PF) [12]. By contrast, the NTV^2 is effective for all loads, but at the cost of additional switching loss [13]. In other words, optimal performance cannot be always achieved by using a unitary PWM over the entire load range. Therefore, the hybrid SVM algorithm incorporating multi-PWM modes has received much attention, especially in industrial applications. For grid-tied photovoltaic (PV) systems, switching sequences have been optimized to minimize the NP voltage ripple [14], suppress the common-mode voltage (CMV) [15]-[17], and intently obtain unbalanced dc-links [18]. In [19] and [20], the NTV and NTV^2 strategies are combined for motor drives. Aiming for the 3L-NPC inverter-fed two-phase induction motor, a hybrid solution with four discontinuous PWM (DPWM) modes is given in [21] to eliminate NP voltage oscillation and lower the switching loss. Nevertheless, it is noticeable that the SVM would bring a higher computational burden while deploying more switching states.

By contrast, the CBPWM strategy is characterized by the simple implementation. Given that the NTV and NTV^2 schemes have their equivalent CBPWM counterparts, the aforesaid issues, such as diverged NP potential and additional switching actions, still exist when exploiting only one type of modulation signal. Hence, the hybrid CBPWM has been in the spotlight in recent years. In [22], a band-limited solution is given to eliminate the NP voltage ripple caused by 2-L switching intervals and reduce power losses resulting from the 3-L ones. With a dual-layer modulation method [23], NP voltages are kept balanced with fast dynamics. In [24], an NP current control method with three degrees of freedom is explored to achieve maximum ripple elimination in the NP. In [25], by adjusting modulation waves, multi-CBPWM schemes are generated to restore drifted NP voltage over a wide frequency range for high-power traction drives. Nevertheless, the above PWM strategies fail to reveal the relationship between hybrid pulse patterns and associated zero-sequence voltage (ZSV). Furthermore, the NP voltage balancing performance is unacceptable at a lower PF angle. In terms of switching losses, 3-L pulse patterns produced by auxiliary signals of the NTV^2 are merely compensated by NTV counterparts. More importantly, no clear advancement of the proposed PWM algorithms in the literature has so far been seen in the studied electric aircraft powertrains with designated MI and PF at different flight stages.

In this paper, a novel hybrid carrier-based virtual-space-vector coordinate-driven (HCBVSVCD) PWM, is proposed for the studied TeDP applications. The sextant-coordinate system is adopted to derive the required ZSV explicitly and simplify the implementation. In low PF operating regions, coordinate-based modulation waves are employed, which can equivalently enable NTV^2 to mitigate NP voltage ripple. To enable a longer flight range with high-efficiency electric propulsion in mild load angles, surplus switching losses rendered by auxiliary signals in decomposition regions are reduced by integrating the coordinate-based active DPWM algorithm seamlessly. This brings constant clamping intervals in 3-L switching regions. In addition, to keep NP voltage balanced, a bias voltage or dual-ZSV is injected into modulation waves.

The rest of this paper is organized as follows. The principles of the aircraft TePD system are presented in Section II. The proposed PWM strategy, together with coordinates mapping, modulation signals reconstruction, dual-ZSV derivation and active NP voltage balancing control is detailed in Section III. The effectiveness of this strategy is verified by simulation and experimental results given in Section IV and Section V. The main conclusions of this work are summarized in Section VI.

II. Principles of Aircraft TeDP System

A. Control Design and Mission Profile of TeDP System

Fig.3 shows the control diagram of the TeDP system studied in this work. To enable all functionalities for thrusting aircraft, the machine speed control, flux-weakening control, droop control and PWM modulator are involved. The speed control regulates the propulsive amount at different stages of flight. The vector control technique is adopted, aiming for controlling flux and torque independently. For regulating the dc current of bipolar EPS, the droop behaviors are used in the control design.

The surface-mounted PMSM is here assumed as an electric propulsion motor fed by the 3-L T^{2}C. The electromagnetic torque manifested by T_{em} is thus determined by:

$$T_{em} = \frac{3}{2} n_p \cdot \varphi_f \cdot i_q \tag{1}$$

where n_p is the pole-pair number. φ_f is the permanent magnet flux linkage. i_q is the q-axis component of motor current.

Besides, the limitation of machine stator voltage, expressed by V_{lim}, satisfies the following equation:

$$(i_d + \frac{\varphi_f}{L_d})^2 + i_q^2 = (\frac{V_{lim}}{\omega_e L_q})^2 \tag{2}$$

where i_d indicates the d-axis components of motor current. L_d and L_q denote the d- and q-axis inductance, respectively. ω_e refers to electrical angular frequency.

To avoid exceeding the capacity of the machine and inverter, the maximum current represented as I_{max} is constrained by:

$$i_d^2 + i_q^2 \le I_{max}^2 \tag{3}$$

To fulfill the constraints set by (2) and (3), the overlapped region of voltage and current circles is the allowable operating point by the TeDP system. Its operating trajectory is depicted in Fig.4(a). As can be seen, to crank the propeller in the startup

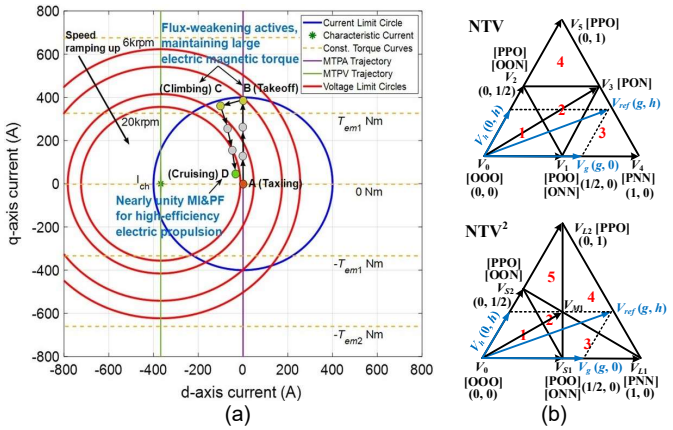

Fig. 4. (a) Operating trajectory of the studied aircraft TeDP system. (b) The SVD of the 3-L topology

TABLE I
SWITCHING PRINCIPLE OF THE 3-L T²C

Switching State	Gating Signals				Output Voltage Level
	S_{x1}	S_{x2}	S_{x3}	S_{x4}	
[P]	1	1	0	0	$V_{dc}/2$
[O]	0	1	1	0	0
[N]	0	0	1	1	$-V_{dc}/2$

process, operating points initially track the maximum torque per amp (MTPA) line from point A, followed by the raised torque currents at the taxiing stage. After that, the aircraft takes off at point B which is followed by injecting large de-fluxing currents at point C to maintain such a large torque along with machine speed ramping up. This reactive power drops the PF down but should be above 0.6 considering the system's efficiency, which is the lowest value during the flight. Due to the torque demand reduction in the high-speed region, the operating point moves towards point D at the cruise, normally with a machine speed of 20 krpm below and a MI of 0.9 above, which attains nearly unity PF. The second half of this mission profile, namely descending and landing stages, can execute aforesaid operating points inversely. Without loss of generality, this study primarily focuses on operating conditions prior to reaching the cruise.

B. Three-Level T-type NPC Topology, Conventional SVM Strategies and Their Associated Issues

As shown in Fig.2, each phase-leg of 3-L T²C is comprised of a half-bridge (HB) switch (S_{x1} and S_{x4}) and a common-source (CS) switch (S_{x2} and S_{x3}), where x={A, B, C}. Two equal capacitors (C_1 and C_2) are series-connected to form the dc-link. The gating signal of S_{x1} is complementary to that of S_{x3}. Likewise, S_{x2} and S_{x4} are on and off alternatively. Thus, there are 27 switching states generated in total. When S_{x1} and S_{x2} are turned on, the switching state is denoted as [P], and the output voltage level is $V_{dc}/2$. The switching state [O] means that the CS switch is turned on, which produces zero output voltage. The switching state [N] indicates that S_{x3} and S_{x4} are turned on, with an output voltage of $-V_{dc}/2$. In this way, zero, small, medium and large vectors are gained to synthesize the reference voltage vector. The switching principle can be found in Table I.

Among the SVM for 3-L topology, the NTV and NTV² are widely-used modulation algorithms, where their space-vector diagram (SVD) of the first sector is shown in Fig.4(b). Based on the analysis in [12], it is known that, due to the adverse impact of the medium vector, the NTV experiences NP voltage drift and low-frequency ripple for certain operating conditions. Though the NTV² leverages multi-segment pulse trains to gain perfect NP potential balance and eliminated capacitor voltage ripple in all loads, extra switching actions render loss issues, particularly for inverters in high-power industrial applications.

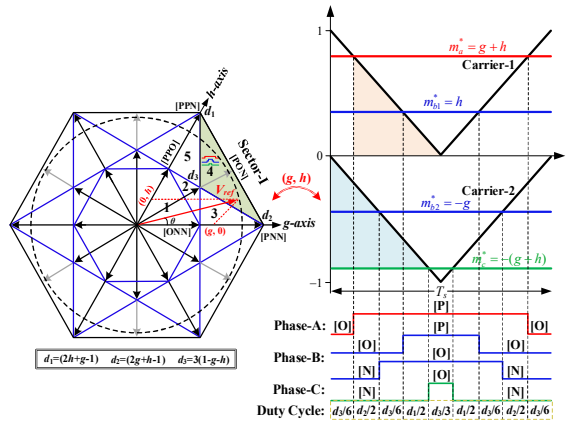

Fig. 5. The relationship between VSV switching patterns and modulation waves under the *g-h* reference frame for subsector-4 of Sector-I.

C. Fast PWM Generation Method with G-H Plane

For multilevel converters, the digital controller may suffer from computational burden when using the SVM. To generate pulse trains more efficiently, via (4), an obliqued reference frame, named the sextant plane, adopts algebraic functions to judge sector/subsector and determine the required duty cycles.

$$\begin{bmatrix} V_g \\ V_h \end{bmatrix} = \begin{bmatrix} 1 & -1/\sqrt{3} \\ 0 & 2/\sqrt{3} \end{bmatrix} \begin{bmatrix} V_\alpha \\ V_\beta \end{bmatrix} \tag{4}$$

where $V_{g\sim h}$ are the magnitudes of space vector in the *g-h* frame.

The coordinates of NTV and NTV² are shown in Fig.4(b). (V_g, V_h) is normalized with a large vector and written as (g, h).

III. PROPOSED HYBRID CARRIER-BASED VIRTUAL-SPACE-VECTOR COORDINATE-DRIVEN PWM STRATEGY

In the following text, the proposed HCBVSVCD modulation technique is introduced in each subsection. Without loss of generality, the first sector is chosen as a representative example to explain and analyze comprehensively.

A. Principle of Carrier-Based Virtual-Space-Vector PWM in Sextant-Coordinate Reference Frame

It is assumed that V_{ref} falls into subsector-4, as illustrated in Fig.4(b). Three-phase modulation signals and their equivalent pulse patterns are presented in Fig.5. With similar triangles, the following equations can be ensured:

$$\begin{cases} \dfrac{V_a^*}{V_{dc}/2} = \dfrac{T_s/2-(1-g-h)\cdot T_s/2}{T_s/2} \\ \dfrac{V_{b1}^*}{V_{dc}/2} = \dfrac{T_s/2-(2g+h-1)\cdot T_s/2-2(1-g-h)\cdot T_s/2}{T_s/2} \\ \dfrac{V_{b2}^*}{-V_{dc}/2} = \dfrac{(2g+h-1)\cdot T_s/2+(1-g-h)\cdot T_s/2}{T_s/2} \\ \dfrac{V_c^*}{-V_{dc}/2} = \dfrac{T_s/2-(1-g-h)\cdot T_s/2}{T_s/2} \end{cases} \tag{5}$$

where V_a^* and V_c^* refer to modulation waves for Phase-A and C, V_{b1}^* and V_{b2}^* are two auxiliary modulation waves for Phase-B, T_s is a switching period, and V_{dc} denotes the dc-bus voltage.

To simplify the calculation further in digital processors, those

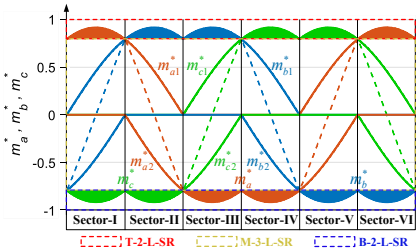

Fig. 6. Division of modulation waves for the CBVSV implementations.

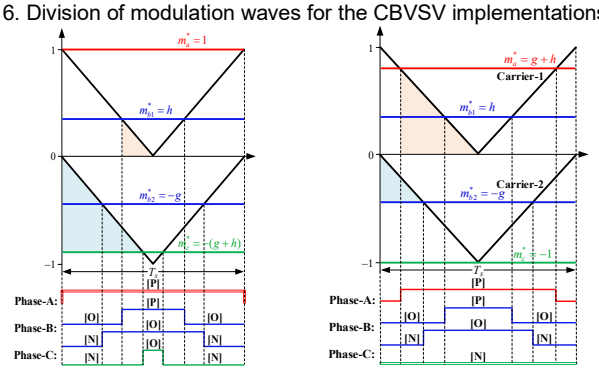

Fig. 7. Modulation waves and associated switching patterns under clamping (a) Phase-A and (b) Phase-C.

modulation signals are nominalized with half of the dc-bus voltage, i.e., $V_{dc}/2$. Therefore, VSV-enabled modulation signals, represented by m_a^*, m_{b1}^*, m_{b2}^* and m_c^*, can be attained as:

$$\begin{cases} m_a^* = g + h & m_{b1}^* = h \\ m_{b2}^* = -g & m_c^* = -(g+h) \end{cases} \tag{6}$$

A similar derivation can be carried out for the rest of the regions within the 3-L SVD, thereby establishing the sextant-coordinate-driven CBPWM with VSV outputs and forming the basis of the proposed modulation technique in this paper.

B. Reconstructed Coordinate-Driven Modulation Waves

It can be seen from Fig.5 that, in contrast with the original SVM method with the seven-segment, the nine-segment pulse train configured by auxiliary modulation signals, i.e., m_{b1}^* and m_{b2}^*, leads to two extra switching actions during a switching period. To compensate for these resultant switching losses in Phase-B, m_a^* and m_c^* would be required to clamp pole voltage to positive or negative dc-rail, respectively.

Prior to reconstructing three-phase modulation waves for the presented coordinate-based VSV PWM in the following, their associated switching region (SR) over a fundamental period can be grouped as: the top 2-L (T-2-L), middle 3-L (M-3-L) and bottom 2-L (B-2-L). The division of the aforesaid intervals is shown in Fig.6. Taking Phase-A as an example, the modulation signal in Sector-I and VI belongs to T-2-L-SR, and that of B-2-L-SR refers to Sector-III and IV. Besides, Sector-II and V correspond to regions with decomposed modulation waves. Similarly, m_{b1}^*, m_{b2}^* and m_{c1}^*, m_{c2}^* are the auxiliary modulation signals of Phase-B and C among other sectors. Consequently, modulation waves sorted by T-2-L-SR and B-2-L-SR can be configured as discontinuous switching patterns.

As the three-phase nominalized sinusoidal signals satisfy:

$$\begin{bmatrix} m_a \\ m_b \\ m_c \end{bmatrix} = \begin{bmatrix} 1 & 1/2 \\ -1/2 & 1/2 \\ -1/2 & -1 \end{bmatrix} \cdot \begin{bmatrix} g \\ h \end{bmatrix} \tag{7}$$

To realize the discontinuous pulse train for Phase-A or C, as

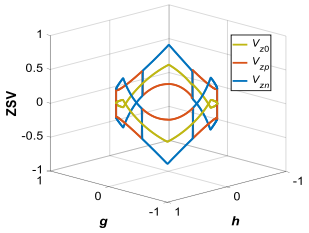

Fig. 8. Coordinated-based ZSVs for the proposed PWM strategy.

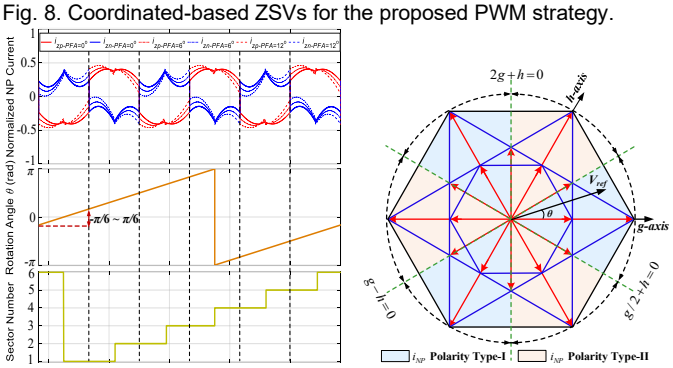

Fig. 9. (a) the correlation among the normalized NP current, rotation angle and sector number under unity MI and different load angles (b) the SVD of the proposed PWM strategy with NP currents polarities.

presented in Fig.7, two types of ZSVs denoted by V_{za} and V_{zc} are preset for the VSV-based modulation waves.

$$V_{za} = 1 - m_a = 1 - g - h/2 \tag{8}$$

$$V_{zc} = -1 - m_c = -1 + g/2 + h \tag{9}$$

In this sense, the g- and h-axis coordinates depending on the modulation depth of the target systems clearly present the ZSV demands if non-switching intervals are deployed during the cruising stage. Besides, characteristics of ZSV in the traditional frequency domain have been extended into vector space.

A similar derivation can be carried out for the rest of the sectors, and is expressed as follows:

$$\begin{cases} V_{zp} = 1 - \underset{i=a,b,c}{\mathrm{MAX}}[m_i(g,h)] \\ V_{zn} = -1 - \underset{i=a,b,c}{\mathrm{MIN}}[m_i(g,h)] \end{cases} \tag{10}$$

where V_{zp} and V_{zn} are defined as the basis ZSV that leads to constant states of [P] and [N] in one phase leg. MAX and MIN represent the maximum and minimum functions, respectively.

After that, dual ZSV sets, manifested by V_z and V_z^*, can be generated by the linear combination, and are written by:

$$\begin{cases} V_z = k \cdot V_{zp} + (1-k) \cdot V_{zn} \\ V_z^* = (1-k) \cdot V_{zp} + k \cdot V_{zn} \end{cases} \tag{11}$$

where k refers to a coefficient and $k \in [0, 1]$.

An interesting finding shows that when k equals 0.5 in (11), written as V_{z0}, a chance to restore the CBVSV strategy can be brought. This means that the proposed modulation technique with reconstructed coordinate-based modulation signals is allowed to send hybrid switching patterns that fit the operating points of the studied aircraft TeDP systems. Fig.8 presents the dedicated ZSVs, as a function of sextant coordinates over a fundamental period, for the presented HCBVSVCD strategy.

C. Active Capacitor Voltage Balancing Control

If the NP voltage error exists, positive or negative dc-rail clamping is required to be chosen properly. It is known that the average NP current over a carrier period can be calculated by

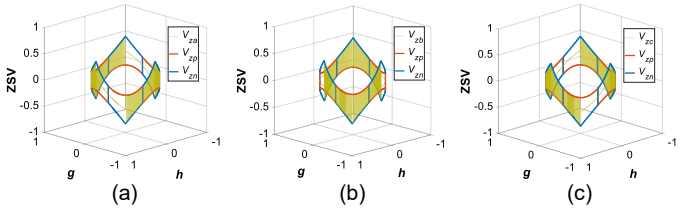

Fig. 10. Dual ZSV sets as a function of *g*- and *h*-axis coordinates for (a) Phase-A (b) Phase-B (c) Phase-C.

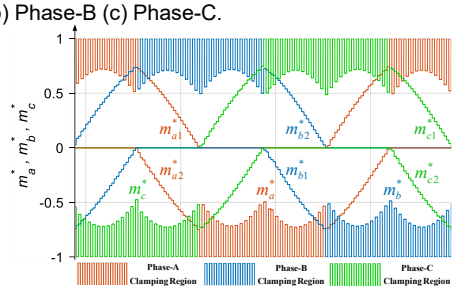

Fig. 11. The three-phase modulation signals of the proposed PWM strategy at the aircraft cruising stage.

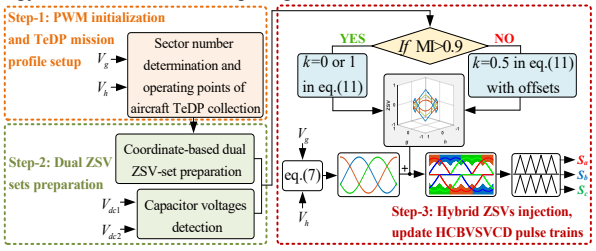

Fig. 12. Flowchart of the proposed HCBVSVCD modulation technique.

$$\overline{i_{np}} = \sum_{x=a,b,c} d_{xo} \cdot i_x \tag{12}$$

where d_{xo} indicates the phase duty cycle that produces [O] state.

With the volts-second principle, d_{xo} can be further expressed:

$$d_{xo} = 1 - \left| m_x^* \right| \tag{13}$$

where m^*_x denotes the three-phase modulation waves.

By substituting (7), (10), (11) and (13) into (12), NP currents produced by the presented algorithm can be analyzed from the perspective of dual ZSV sets. Fig.9(a) shows the correlation among the normalized NP current, rotation angle of reference voltage vector and sector number under unity MI and different power factor angles (PFAs). As shown, the polarities of NP currents generated by V_{zp} and V_{zn}, denoted as i_{zp} and i_{zn}, alternatively vary in every π/3 radian when the load angle is near null, indicating the assignment of 0 or 1 for k in (11) periodically. Fig.9(b) elaborates on this discrepancy in the SVD of the proposed PWM technique. Due to the much-upscaled output active power during cruising, the above scenario fits the operating points of the mission profile of the studied TeDP systems. Then, a dual ZSV-set is hence injected into three-phase modulation signals of the coordinate-based CBVSV according to the NP voltage drift tendency. Fig.10 plots three-dimensional (3D) ZSVs injection regions for balancing NP potential. The resultant modulation waveforms of the proposed HCBVSVCD at the cruise stage are shown in Fig.11. As shown, phase legs have been periodically clamped in specific switching intervals between positive and negative dc-rail, thus reducing switching actions against the prior VSVs caused. In the case of the remaining operating points, featuring less than a MI of 0.9, by tuning the dwell time of small vectors, reference voltage

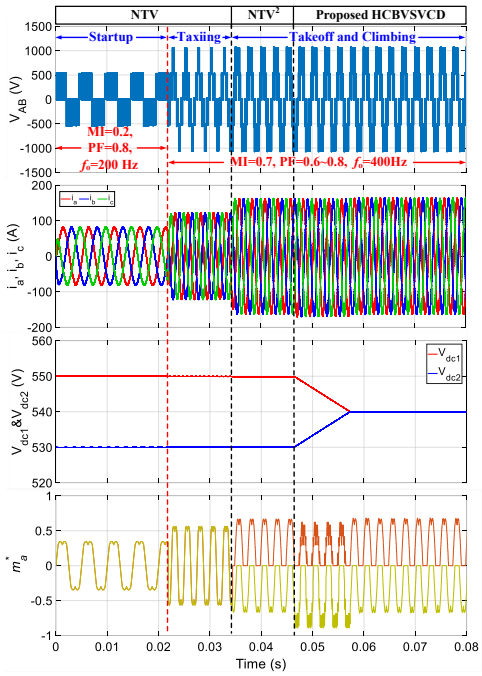

Fig. 13. Simulation results for the studied TeDP systems executing the multiple processes of the startup, taxiing, takeoff and climbing.

offsets can be derived and injected into (6), accordingly.

Fig.12 presents the flowchart of the proposed HCBVSVCD modulation strategy for the target propulsion drive applications.

IV. Simulation Results

The simulation model of the developed 3-L T²C-based MW-scale aircraft TeDP system is built in the Simulink/PLECS environment with parameters listed in Table II. To verify the NP voltage balance, output variable distortion and losses of the proposed PWM, the NTV and NTV² schemes are chosen as the benchmark in the following. The operating conditions with two sets of fundamental frequencies, modulation indices and power factors, referring to the takeoff, climbing, and cruising stage of the target systems, are tested in the simulations.

A. Capacitor Voltage Balancing Capability

As the studied systems feature a variable frequency ac output, the ability of NP voltage balancing is first tested during the initial stage of turboelectric propulsion. As shown in Fig.13, upper and lower-side capacitor voltages are set at 550 V and 530 V, respectively. During the startup process with a MI of 0.2, a PF of 0.8 and a fundamental frequency (f_0) of 200 Hz, a steady dc voltage offset constantly exists in the NP. This imbalance will also last during taxiing, takeoff and climbing, which refers to a MI of 0.7 and PF ranging from 0.6 to 0.8 in the flux-weakening region, and a f_0 of 400 Hz. As for the NTV² in the above case, the NP potential divergence remains until the proposed strategy is adopted. This implies that dedicated pulse trains can be produced to correct the error. Regarding the capability of NP potential balancing in the thrust generation stage, which corresponds to a MI of 0.9 and an average PF of 0.95 under a f_0 of 1 kHz, Fig.14 shows the results after using the NTV, NTV² and proposed HCBVSVCD. As shown, the NTV and NTV² are both ineffective in recovering capacitor voltages. Besides, the NTV scheme leads to a low-frequency capacitor voltage fluctuation. By contrast, the perfect balance process can

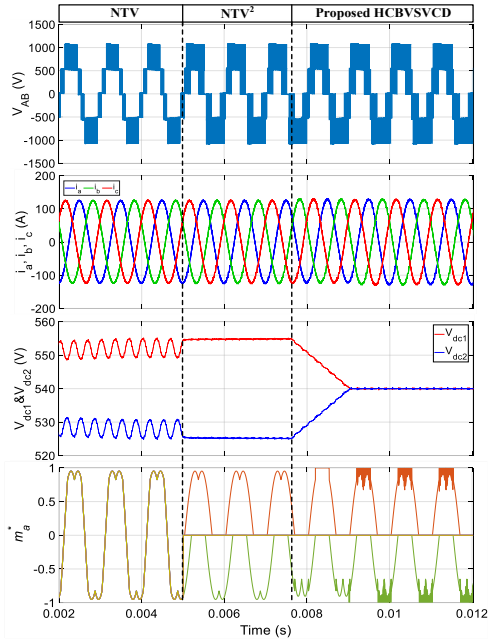

Fig. 14. Simulation results for the studied TeDP systems generating steady propulsion (MI=0.9, PF=0.95 and f_0=1 kHz).

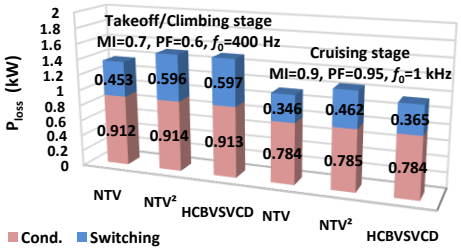

Fig. 15. Power loss breakdown comparison using the conventional NTV, NTV² and the proposed HCBVSVCD under two operational modes.

be realized by deploying the proposed PWM algorithm.

B. Output Variables Performance

Over a switching period, the primary output variables are three-phase modulation waves. Taking Phase-A as an example, as shown in Figs.13 and 14, to gain 3-L switching intervals as same as the NTV², the presented scheme decomposes its coordinate-based PWM signals periodically. With the addition of NP voltage offsets or ZSVs in those waves, modulated variables can be flexibly adapted based on the imbalance.

Over a fundamental period, one of the key output variables that determine the modulation performance is the phase current. In terms of Phase-A, the total harmonic distortion (THD) of the proposed HCBVSVCD solution during takeoff and climbing is 1.15%. In comparison with that, the THD by the NTV² at the same stage is 1.23%. The slight increase amount is because of the shifted NP voltage. For the cruising stage, the THD by the introduced PWM technique is 2.47%, while this metric by the original NTV² is 1.95% under the same conditions. The reason for that is discontinuous pulse trains are adopted in addition to phase decomposed regions. As none of the 3-L switching intervals and phase clamping regions, a THD of 1.25% is attained by the NTV, which ranks as the lowest amount.

C. Power Loss Analysis

To be consistent with the hereafter experimentations, the semiconductor's power losses by different PWM strategies are analyzed by the applied Cree/Wolfspeed HT-3000 series 900 V silicone-carbide (SiC) module which builds for the 3LT²C prototype. Two representative operating points for the TeDP systems in the takeoff/climbing and cruising are chosen here to discuss. The switching frequency is set to be 30 kHz, the dc-bus voltage is 540 V and the power rating is 200 kVA. Using characteristic curves in the manufacturer's datasheet, the power losses can be calculated by the PLECS simulation tools.

Fig.15 shows the results of conduction and switching losses by the NTV, NTV² and the proposed HCBVSVCD strategies under associated operational modes of the target drives. As shown, prior to entering the steady-state of the TeDP systems, the presented scheme produces a quite close power loss amount compared with the NTV², aiming to eliminate NP voltage ripple and keep NP voltage balanced under a period of lower PFs. But, when generating turboelectric propulsion, the proposed PWM method leverages discontinuous pulse patterns and shows its advantages over sole-used auxiliary modulation signals which the extra switching losses attribute to. Although the NTV scheme features the least thermal issue, it is arduous to apply considering its potential risk of jeopardized onboard capacitor bank lifetime and semiconductors over-voltage stress failure.

D. Comparison With Other Hybrid Modulation Strategies for Three-Level NPC Converters

Compared with the 3L hybrid PWM for NPC topologies, the presented technique has the following attractive characteristics:

1) With the generic ZSV in the sextant-coordinate system, the HCBVSVCD is favorable to modify NTV²-oriented switching patterns, thus simplifying modulation processes and fitting for the TeDP system with wide-range operating conditions. However, the computational burden is raised by SV implementation in [14]-[19].
2) For NP voltage balancing control, by simply injecting dual-ZSV or offsetting modulated waves, the proposed scheme can recover shifted NP voltage. Due to medium vectors, methods in [15]-[17] cause NP voltage ripple. Though the study in [23] that highly depend on four-quadrant parameters gains net-zero NP current, it might render complexity to the target drives with multi-operational modes. The works of [24] use three degrees of freedom to correct the error, but the sampling delay might be an issue for low carrier-ratio applications.
3) Owing to the configuration of phase-clamping regions, the VSV outputs incorporate discontinuous pulse trains to reduce switching actions, thereby lowing those power losses that 3-L switching intervals produce. By contrast, the study in [20] has a shortcoming in this aspect.
4) In view of the equivalence of SVM, the HCBVSVCD would expect to evolve into synchronized PWM easily when the sequence of the reference voltage vector is designed to satisfy the symmetric voltage waves. Unlike [25], carriers are set up in the fall or rising direction.

Nonetheless, it is noted that the studies in [14] and [20] can reduce CMV, while this will be optimized in our future works.

V. Experimental Results

Before an MW-class high-speed electric propulsion motor is available to serve as the power load to validate the modulation

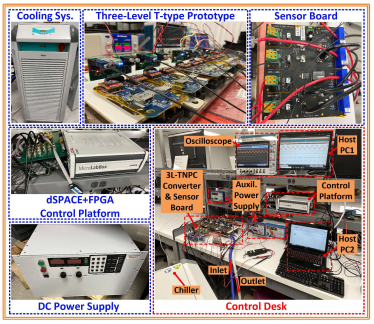

Fig. 16. Experimental test rigs.

TABLE II
AIRCRAFT TEDP SYSTEM PARAMETERS

Parameters	Simulation	Experimentation
Rated power	1000 kVA	200 kVA
DC bus voltage	± 540 V	± 270 V
Switching frequency	30 kHz	30 kHz
Fundamental frequency (f_0)	≤ 1 kHz	≤ 1 kHz
Capacitance (C_1=C_2)	900 μF	300 μF
Modulation index (MI)	≤ 0.95	≤ 0.95
Power factor (PF)	0.6~1.0	0.6~1.0

performance of the proposed HCBVSVCD, the PWM strategy is experimentally tested on a scale-down 200 kVA SiC-based 3-L T^{2}C prototype with specifications detailed in Table II for electric aircraft propulsion applications, as shown in Fig.16. A Magna-Power programmable dc power supply is connected to the dc-link of the converter and an RL load bank is connected to its ac side, which imitates the onboard EPS and PFAs of the assumed high-power density electric machine. A cold plate installed underneath the converter along with a Julabo FL2503 supplying recirculating chilled water consists of the cooling system. The controller includes a dSPACE MicroLabBox and an Intel Max-10 FPGA. The ac side parameters are monitored by a Yokogawa WT5000 precision power analyzer. As the direction of phase current changes rapidly in light-load conditions, it could impair the NP voltage balance capability, experimental tests mainly focus on the studied TeDP systems operating in light-load conditions with variable output f_o.

A. Steady-State Experiments

In terms of the steady-state performance of the proposed HCBVSVCD, the experimentation is firstly tested when the target systems operate in a MI of 0.4 and a PF of 0.8 under a f_o of 400 Hz, which refers to the turboelectric engine startup process. Apart from that, the cruising stage, characterized by a MI of 0.9, a PF of 0.95 and a f_o of 1 kHz, is tested. Fig.17 presents the above results, in which line-to-line voltage features three and five-level in low and high MI regions, respectively. It can be also seen that ac output phase currents are sinusoidal, and two capacitor voltages are maintained at a balanced state.

B. Transient-State Experiments

To validate the dynamic performance of the introduced HCBPWM algorithm for the wide-range operation of the TeDP system, the MI or f_o is carried out an instant change. Fig.18(a) shows that the operating point of MI increases from 0.4 to 0.9. As shown, output variables, such as line-to-line voltage, phase current and capacitor voltages perform well though the amount of phase current raises promptly after altering MI. Fig.18(b) shows the experimental results when the f_o raises from 800 Hz to 1 kHz, which mimics the speed ramping-up process of the

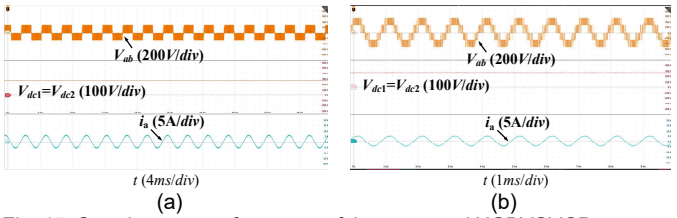

Fig. 17. Steady-state performance of the proposed HCBVSVCD strategy at (a) MI=0.4, PF=0.8 and f_0=400 Hz (b) MI=0.9, PF=0.95 and f_0=1 kHz.

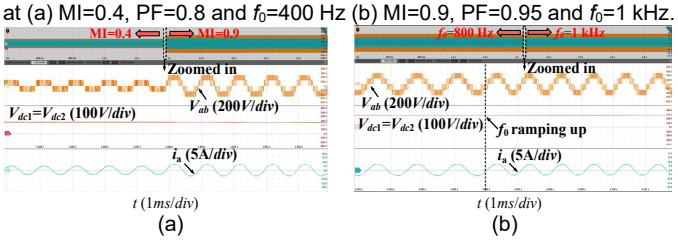

Fig. 18. Transient-state performance of the proposed HCBVSVCD strategy under a step change of (a) MI and (b) f_0.

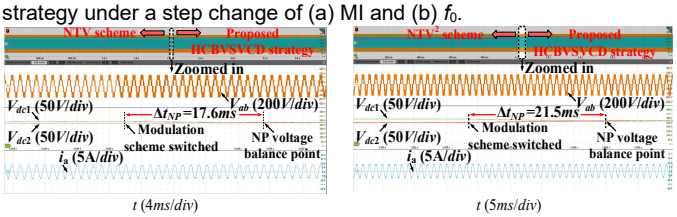

Fig. 19. NP voltage balancing performance of the proposed HCBVSVCD strategy compared with (a) The NTV scheme (b) The NTV^2 scheme.

drive systems. As shown, a smooth transition can be gained in terms of non-shifted NP voltages, sinusoidal phase current and symmetric line-to-line voltage. The aforesaid tests validate a smooth transient performance of the proposed approach.

C. Capacitor Voltage Balancing Performance

To demonstrate the NP voltage balancing performance of the proposed PWM technique, two scenarios are investigated here accordingly. The first case, leading to an NP potential divergence of 15 V, is carried out when the prototype systems imitate the takeoff and climbing stage under a MI of 0.7 and a PF of 0.6, as shown in Fig.19(a). It is evident that two deviated capacitor voltages rendered by the NTV can be quickly restored after the HCBVSVCD scheme is activated within 17.6ms. The other one refers to the case where the propulsion drives generate steady propulsion during the cruise, presenting an operating point of a MI of 0.9 and a PF of 0.95. Prior to sending the presented hybrid pulse patterns, an initial NP voltage imbalance of 40 V is pre-set when employing the NTV^2. In Fig.19(b), as shown, this NP voltage error exists until the proposed algorithm removes the error and keeps the NP voltage balanced again after 21.5ms, altogether with the recovery of distorted phase voltage and current. The aforesaid results are in good agreement with the analysis and design of NP voltage balance control for the variable operating points of TeDP mission profile.

D. Distortion Analysis

By using the FFT analysis, the harmonic contents of NP voltage ripple with different modulation strategies are obtained for the thrust-generation stage and are shown in Fig.20. As can be seen, the NTV scheme leads to the highest amount of dc imbalance in the midpoint of NP, also the 3rd-harmonics is prominent. Besides, although the conventional NTV^2 scheme eliminates low-frequency harmonics, a dc-bias of 1.65 V exists due to the unsymmetric circuit parameters. By contrast, as for

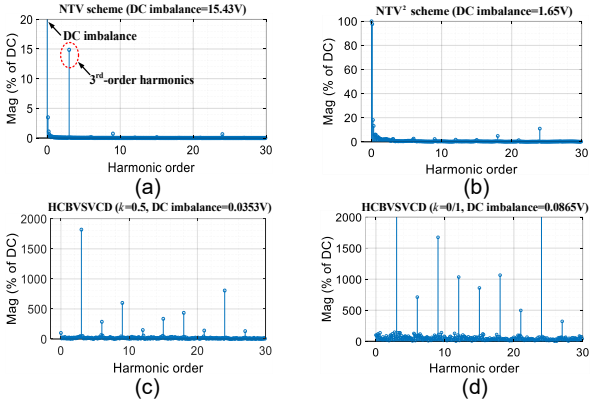

Fig. 20. FFT analysis of NP voltage ripple at the cruise of the TeDP system under (a) The NTV (b) The NTV^2 (c) The proposed HCBVSVCD with k=0.5 (d) The proposed HCBVSVCD with k=0 or 1.

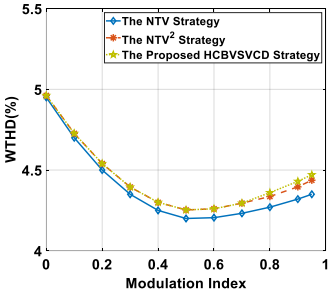

Fig. 21. WTHD of the line-to-line voltage under the NTV, NTV^2 and the proposed HCBVSVCD strategies at different modulation indices.

the presented modulation algorithm, not only the low-frequency harmonics are minimized, but also the discrepancy of capacitor voltages is removed effectively. THD of phase current with the NTV, NTV^2 and the proposed HCBVSVCD are 4.31%, 5.26% and 5.63%, respectively. On the other hand, the weighted THD (WTHD) plotted in Fig.21 shows the line-to-line voltage distortion curve with deepened MI. Compared with each trend, it is seen that the lowest value appears around a MI of 0.5. The reason for that is the nearest SVs or VSVs are used to compose the reference space vector essentially. Due to the equivalence between the NTV^2 and the HCBVSVCD before modifying modulation signals, their WTHD curve merges together until the discontinuous pulse trains are incorporated.

E. Computational Performance

The execution time of all discussed modulation algorithms is measured by the applied control kit. The test results show that it takes 12.4 μs to implement the proposed PWM while 18.7 μs and 21.2 μs are required for the NTV and NTV^2, respectively. This indicates that over 30% and 40% computational time reduction is achieved when using the HCBVSVCD scheme.

I. Conclusion

A new hybrid carrier-based virtual-space-vector modulation technique was proposed in this paper for a 3LT^{2}C in the next-generation TeDP systems. The modulation signals are adapted from the perspective of the aircraft's mission profile. The main contributions of this work are as follows: 1) A generic ZSV in the sextant coordinate system is derived to bring a chance of seamless modulation transition. 2) With an offset of modulated waves or dual-ZSV injection, the capacitor voltage imbalance can be corrected at the variant operating points. 3) The twice-switching regions are leveraged with the help of discontinuous pulse trains, aiming to lower extra switching losses caused by multi-segment intervals. 4) The complexity of hybrid switching patterns is reduced through carrier-based implementation. This PWM algorithm can also apply to other 3L-NPC topologies and establish a cornerstone in future MW-class high-power density motor drives for electric aircraft propulsion applications. Simulation and experimental results confirmed the good overall modulation performance of the proposed scheme in terms of NP voltage ripple, balance, losses, ease of use and high scalability.

References

[1] S. Sirimanna, T. Balachandran, N. Salk, J. Xiao, D. Lee and K. Haran, "electric propulsors for zero-emission aircraft: partially superconducting machines," *IEEE Electrific. Mag*., vol. 8, no. 2, pp. 18-26, Jun. 2020.

[2] P. Wheeler *et al*., "Electric/hybrid-electric aircraft propulsion systems," *Proc. IEEE*, vol. 109, no. 6, pp. 1115-1127, Jun. 2021.

[3] M. T. Fard, J. He, H. Huang and Y. Cao, "Aircraft distributed electric propulsion technologies - a review," *IEEE Trans. Transport. Electrific*., doi: 10.1109/TTE.2022.3197332.

[4] European Commission, "Directorate-general for mobility and transport," 2015. [Online]. Available: https://ec.europa.eu/transport/sites/transport/files/modes/air/doc/flightpath2050.pdf

[5] M. Ghassemi, A. Barzkar and M. Saghafi, "All-electric NASA N3-X aircraft electric power systems," *IEEE Trans. Transport. Electrific*., doi: 10.1109/TTE.2022.3158186.

[6] E-Fan X - Electric flight - Airbus, [Online] https://www.airbus.com/innovation/zero-emission/electric-flight/e-fan-x.html.

[7] "STARC-ABL" NASA Glenn Research Center. [Online]. Available: https://www1.grc.nasa.gov/aeronautics/eap/airplane-concepts/starc-abl/

[8] S. Bozhko *et al*., "Development of aircraft electric starter–generator system based on active rectification technology," *IEEE Trans. Transport. Electrific*., vol. 4, no. 4, pp. 985-996, Dec. 2018.

[9] H. Abu-Rub *et al*., "Medium-voltage multilevel converters—state of the art, challenges, and requirements in industrial applications," *IEEE Trans. Ind. Electron.*, vol. 57, no. 8, pp. 2581-2596, Aug. 2010.

[10] S. Belkhode, A. Shukla and S. Doolla, "Split-output hybrid active neutral-point-clamped converter for MV applications," *IEEE J. Emerg. Sel. Topics Ind. Electron*., vol. 2, no. 2, pp. 184-195, Apr. 2021.

[11] J. Shen, S. Schröder, R. Rösner, and S. El-Barbari, "A comprehensive study of neutral-point self-balancing effect in neutral-point-clamped three-level inverters," *IEEE Trans. Power Electron*., vol. 26, no. 11, pp. 3084–3095, Nov. 2011.

[12] N. Celanovic and D. Boroyevich, "A comprehensive study of neutral-point voltage balancing problem in three-level neutral-point-clamped voltage source PWM inverters," *IEEE Trans. Power Electron*., vol. 15, no. 2, pp. 242-249, Mar. 2000.

[13] S. Busquets-Monge, J. Bordonau, D. Boroyevich and S. Somavilla, "The nearest three virtual space vector PWM-a modulation for the comprehensive neutral-point balancing in the three-level NPC inverter," *IEEE Power Electron. Lett.,* vol. 2, no. 1, pp. 11-15, Mar. 2004.

[14] Y. Li *et al*., "Neutral-point voltage analysis and suppression for NPC three-level photovoltaic converter in LVRT operation under imbalanced grid faults with selective hybrid SVPWM strategy," *IEEE Trans. Power Electron.*, vol. 34, no. 2, pp. 1334-1355, Feb. 2019.

[15] M. Lak *et al*., "A hybrid method to eliminate leakage current and balance neutral point voltage for photovoltaic three-level T-type inverter," *IEEE Trans. Power Electron*., vol. 36, no. 10, pp. 12070-12089, Oct. 2021.

[16] T. Yu, W. Wan and S. Duan, "A modulation method to eliminate leakage current and balance neutral-point voltage for three-level inverters in photovoltaic systems," *IEEE Trans. Ind. Electron*., vol. 70, no. 2, pp. 1635-1645, Feb. 2023.

[17] C. Qin, X. Xing and Y. Jiang, "Hybrid space vector modulation scheme to reduce common-mode voltage magnitude and frequency in three-level quasi-Z-source inverter," *IEEE J. Emerg. Sel. Topics Power Electron*. doi: 10.1109/JESTPE.2021.3137609

[18] X. Wu, G. Tan, G. Yao, C. Sun and G. Liu, "A hybrid PWM strategy for three-level inverter with unbalanced DC links," *IEEE J. Emerg. Sel. Topics Power Electron*., vol. 6, no. 1, pp. 1-15, Mar. 2018.

[19] W. Jiang, S. Du, L. Chang, Y. Zhang, Q. Zhao, "Hybrid PWM strategy of SVPWM and VSVPWM for NPC three-level voltage-source inverter," *IEEE Trans. Power Electron.*, vol. 25, no. 10, pp. 2607-2619, Oct. 2010.

[20] F. Guo *et al*., "Hybrid active modulation strategy for three-level neutral-

point-clamped converters in high-speed aerospace drives," *IEEE Trans. Ind. Electron*. doi: 10.1109/TIE.2022.3176309
[21] G. Zhang *et al*., "Hybrid discontinuous space vector PWM strategy for three-level inverters under two-phase loads condition," *IEEE Trans. Power Electron.*, vol. 37, no. 2, pp. 1711-1721, Feb. 2022.
[22] N. Beniwal, *et al*., "Band-limited three-level modulation for balancing capacitor voltages in neutral-point-clamped converters," *IEEE Trans. Power Electron.*, vol. 35, no. 9, pp. 9737-9752, Sept. 2020.
[23] N. Beniwal *et al*., "Dual-layer pulsewidth modulation technique for average neutral point current control in NPC converters," *IEEE Trans. Power Electron*., vol. 37, no. 10, pp. 11762-11773, Oct. 2022.
[24] Z. Dong *et al*., "A hybrid modulation method with the maximum controllable range of the neutral-point current for three-level NPC," *IEEE Trans. Transport. Electrific*., doi: 10.1109/TTE.2022.3176271
[25] Z. Gao *et al*., "Hybrid improved carrier-based PWM strategy for three-level neutral-point-clamped inverter with wide frequency range," *IEEE Trans. Power Electron.*, vol. 36, no. 7, pp. 8517-8538, Jul. 2021.

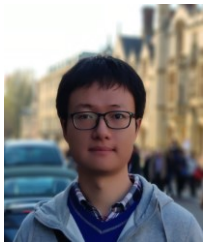

Feng Guo (Member) received his Ph.D. degree in electrical and electronics engineering from the University of Nottingham, Nottingham, U.K., in 2021. Since January 2022, he has been with the University of Arkansas, Fayetteville, AR, USA, as a Postdoctoral Fellow. His research interests include control and modulation of multilevel converters, wide-bandgap device applications, high-speed motor drives and transportation electrification, etc. He is the recipient of the 2022 IEEE Industry Applications Society Transactions Second Place Prize Paper Award.

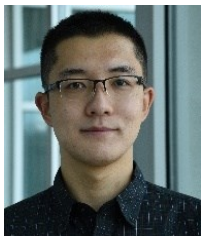

Zhuxuan Ma (Student Member) received the B.S. degree in electrical engineering from the Beijing Institute of Technology, Beijing, China, in 2017, and the M.S. degree from The Ohio State University, Columbus, OH, USA, in 2019. He is currently working towards the Ph.D. degree at the University of Arkansas, Fayetteville, AR, USA. His current research interests include multilevel inverters, wide bandgap power devices, etc.

Fei Diao (Student Member) received the B.E. and M.E. degrees in electrical engineering from Southwest Jiaotong University, Chengdu, China, in 2015 and 2018, respectively. He is currently working toward the Ph.D. degree with the University of Arkansas, Fayetteville, AR, USA. His main research interests include modulation and control of power converters and wide bandgap (WBG) power device applications.

Yue Zhao (Senior Member) received a Ph.D. degree in electrical engineering from the University of Nebraska-Lincoln, Lincoln, USA, in 2014. He is an Associate Professor in the Department of Electrical Engineering at the University of Arkansas, Fayetteville, USA.
Dr. Zhao is an Associated Editor of the IEEE Transactions on Industry Applications and IEEE Open Journal of Power Electronics. He was a recipient of 2018 NSF CAREER Award and the 2020 IEEE IAS Andrew W. Smith Outstanding Young Member Achievement Award.

Patrick Wheeler (Fellow) received his BEng (Hons.) and PhD degree in electrical engineering from the University of Bristol, U.K., in 1990 and 1994, respectively. He was Head of the Department of Electrical and Electronics Engineering at the University of Nottingham from 2015 to 2018. He is currently the Head of the Power Electronics, Machines and Control Research Group of the University of Nottingham, Nottingham, U.K. He is a member of the IEEE PELs AdCom and is currently an IEEE PELS Vice-President.